Received: 22 January 2026 | Revised: 20 February 2026 | Accepted: 24 February 2026

DOI: 10.1002/rpm2.70050

RESEARCH ARTICLE

RESPONSIVE MATERIALS Open Access WILEY

Super-capacitive carbon materials with large micropores and rich mesopores synthesized using N, S co-doped carbon dots as self-templates

Xi-Rong Zhang | **Hao-Wen Sun** | **Ling Xiao** | **Zhao-Fan Wu** | **Huan-Ming Xiong**

Department of Chemistry, Shanghai Key Laboratory of Electrochemical and Thermochemical Conversion for Resources Recycling, Fudan University, Shanghai, China

Correspondence
Huan-Ming Xiong.
Email: hmxiong@fudan.edu.cn

Abstract

The self-template approach to porous carbon utilizes the precursor's inherent skeletal structure to form pores. When the initial pore sizes in precursors are very small, the final pore sizes of the resulting porous carbon decrease further, because the pores usually collapse during high-temperature calcination. In the case of carbon dots (CDs) as nanosized self-templates, the pores primarily arise from the splintering of CDs, and the resulting pore sizes are usually less than 1 nm. To enlarge the pore sizes and produce more mesopores, nitrogen-sulfur co-doped carbon dots (NSCDs) are designed that utilize the synergistic pore-forming effect of amide bonds and sulfur-containing functional groups. Amide bonds can be broken by alkaline soaking to produce pores, while sulfur groups can decompose into gas during calcination to enlarge pores. After CDs self-assembly, alkaline treatment and calcination, a series of hierarchical porous carbon materials are synthesized with a pore size distribution concentrated in the 1.1–1.6 nm range and an impressive mesopore volume ratio up to 47.2%. The symmetric supercapacitors assembled by such porous carbon exhibit the optimal energy density of 17.3 Wh kg^{-1} at a high-power density of 7000 W kg^{-1}. This study provides a method to tune the pore sizes of carbon electrodes using CDs as self-templates, so as to meet the requirement of supercapacitors working under different conditions.

Keywords
carbon dot, hierarchical porous carbon, self-template, supercapacitor

1 | INTRODUCTION

Porous carbon materials, owing to their large surface area, moderate conductivity and excellent stability, are the most popular electrode materials for electrochemical supercapacitors.[1–3] Among various parameters of porous carbon, the preferred pore structure is the dominant factor for its electrochemical performance, which requires the suitable distribution of different pore sizes, the reasonable volumes of the preferred pores, and the balanced pore density in the whole material. Besides, the chemical composition of the pore surfaces is also important, including the surface groups and the doped elements, that determines the interface impedance, the wetting property and the pseudocapacitance of the electrode.

The preparation methods for porous carbon include physical activation, chemical activation, and templating synthesis, each with its own merits and shortcomings.[4–10] Physical activation is environmentally friendly and cost-effective, but the resulting products usually have low

specific surface areas. Chemical activation can produce a high specific surface area, but the resulting carbon materials are usually microporous, and the assembled supercapacitors perform poorly at high rates due to the lack of mesopores. Moreover, traditional carbonization-activation methods for porous carbon cannot control the pore structures precisely, leading to a broad and random pore size distribution. As for the templating methods, the hard templates can precisely control pore sizes but require cumbersome processes to remove templates completely, while the soft templates are easy to remove but risk the structural collapse. Fortunately, the self-templating methods simplify the fabrication process, because the precursors act as both the templates and the building blocks of the final products, so that the template removing processes are never required. This approach allows for the creation of more complex pore structures, such as the critical hierarchical pores for supercapacitors, but designing and screening the suitable precursors are full of challenges.

Carbon dots (CDs) are a class of nanoscale carbon-based materials (typically smaller than 10 nm) that have attracted major attention because they combine low cost, easy synthesis, and strong photoluminescence.[11–13] CDs not only have excellent solubility in various solvents, enabling homogeneous dispersion in the matrix, but also possess tunable surface states and the ability to incorporate heteroatoms into the carbon framework.[14–16] The porous carbon materials synthesized using CDs as templates exhibit superior electrochemical performance, including capacitance and stability, due to the uniformity and controllability of their pore structures.[17] In our previous reports, CDs were used as self-templates to prepare porous carbon with a pore size distribution concentrated in the sub-nanometer range (0.5–1.0 nm).[18,19] This singular and narrow microporous structure cannot provide continuous mesoporous channels for fast ion transport, thereby lacking responsive ability to the rapid reaction kinetics. To address this issue, it is crucial to find a novel pore-forming mechanism for CDs self-templating, which facilitates the formation of hierarchical porous carbon with the crosslinked large micropores (1–2 nm) and rich mesopores (>2 nm).

In the present research, we combined N, S co-doped CDs (NSCDs) with poly(ethylene glycol) diglycidyl ether (PEGDGE) molecules via an amine-epoxy ring-opening reaction to form a series of polymer hydrogels (NSCD@PHs). These precursors were subsequently treated by alkaline etching and thermal processing to yield a series of carbonized polymer hydrogels (CPHs). NSCDs as self-templates produced micropores of 1.1–1.6 nm in the carbon material, along with a mesopore volume ratio approaching 50%, through the synergistic decomposition effect of amide structures and sulfur-containing functional groups. The symmetric supercapacitor (SSC) assembled by such porous carbon electrodes exhibits high energy density, excellent rate capability, and outstanding cycling stability.

2 | RESULTS AND DISCUSSION

The preparation process of this unique carbon material is illustrated in Scheme 1, where NSCDs serve as crosslinkers, pore-forming agents, and heteroelement dopants simultaneously. At first, NSCDs were synthesized via hydrothermal reaction between L-cysteine and polyethylenimine (PEI). Different amounts of NSCDs were then mixed with PEGDGE to conduct the amine-epoxy ring-opening polymerization at 80°C, which produced the hydrogel precursor NSCD@PHs. Subsequently, the hydrogel was etched in KOH aqueous solution that disrupted the amide bonds in the CDs, creating initial pores within the hydrogel matrix. Since the hot alkaline treatment did not destroy the crosslinking sites between NSCDs and PEGDGE, and NSCDs crosslinked PEGDGE at a high degree, the hydrogel maintained a robust backbone after the alkaline treatment. Finally, the alkali-treated hydrogel was washed, dried, and annealed in a nitrogen atmosphere, during which the initial pores were enlarged by the generated gas, especially from the decomposition of sulfur-containing species. As a result, the hierarchical porous carbon materials (CPHs) were fabricated by the self-templating of NSCDs. By adjusting the amount of NSCDs during the hydrogel preparation, a series of samples (CPH-x, where x denotes the amount of NSCDs added) were obtained to investigate the role of NSCDs in pore formation. Control groups (named Control I, II, and III) were established for parallel investigation on the effects of alkaline etching and zinc chloride respectively, which leads to the intrinsic pore-forming mechanism.

High-resolution transmission electron microscopy (HRTEM) was employed to investigate the structural characteristics of NSCDs. In Figure 1a, NSCDs have diameters of about 3 nm with a lattice fringe spacing of 0.21 nm, corresponding to the (100) planes of graphite.[20,21] In the X-ray diffraction (XRD) patterns (Figure 1b), the doping of larger radius elements into the carbon matrix causes a leftward shift of the (002) diffraction peak, and the broad diffraction peak suggests the low crystallinity of CDs.[22,23] Fourier transform infrared (FTIR) spectroscopy (Figure 1c) reveals vibration bands at around 3425, 1545–1750, 1392, and 1125 cm^{-1}, which correspond to O-H/N-H, C=C/C=O, C-N, and C-O/C-S functional groups, respectively.[24] This indicates that the NSCDs have rich amide linkages, amine groups, and sulfur-containing functional groups. After the amide bonds were cleaved by KOH etching, the structural defects in the NSCDs would split these nanoparticles at high temperature. The blue emission of NSCDs decreases sharply after etching in the photoluminescence (PL) spectra (Figure 1d), which is likely caused by the combined effects of etching-induced changes in graphitic conjugation and the alteration of surface functional groups. To further analyze the surface composition, X-ray photoelectron spectra (XPS) of NSCDs were measured, which showed the atomic ratios of 66.8%, 18.0%, 11.1%, and 4.2% for C, N, O, and S in the

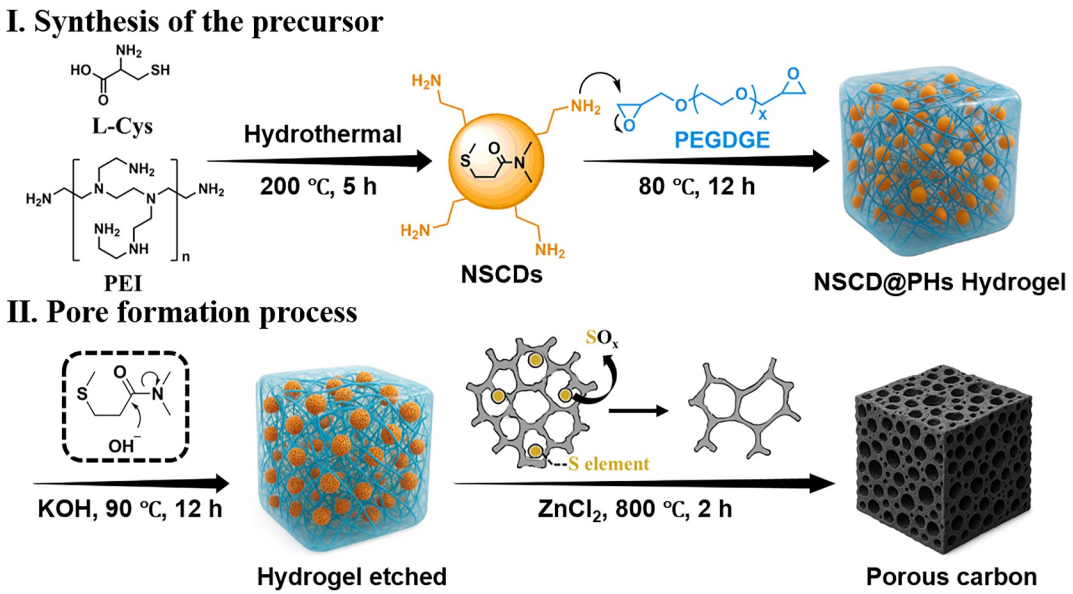

SCHEME 1 Schematic diagram of the synthetic procedure for carbonized polymer hydrogels.

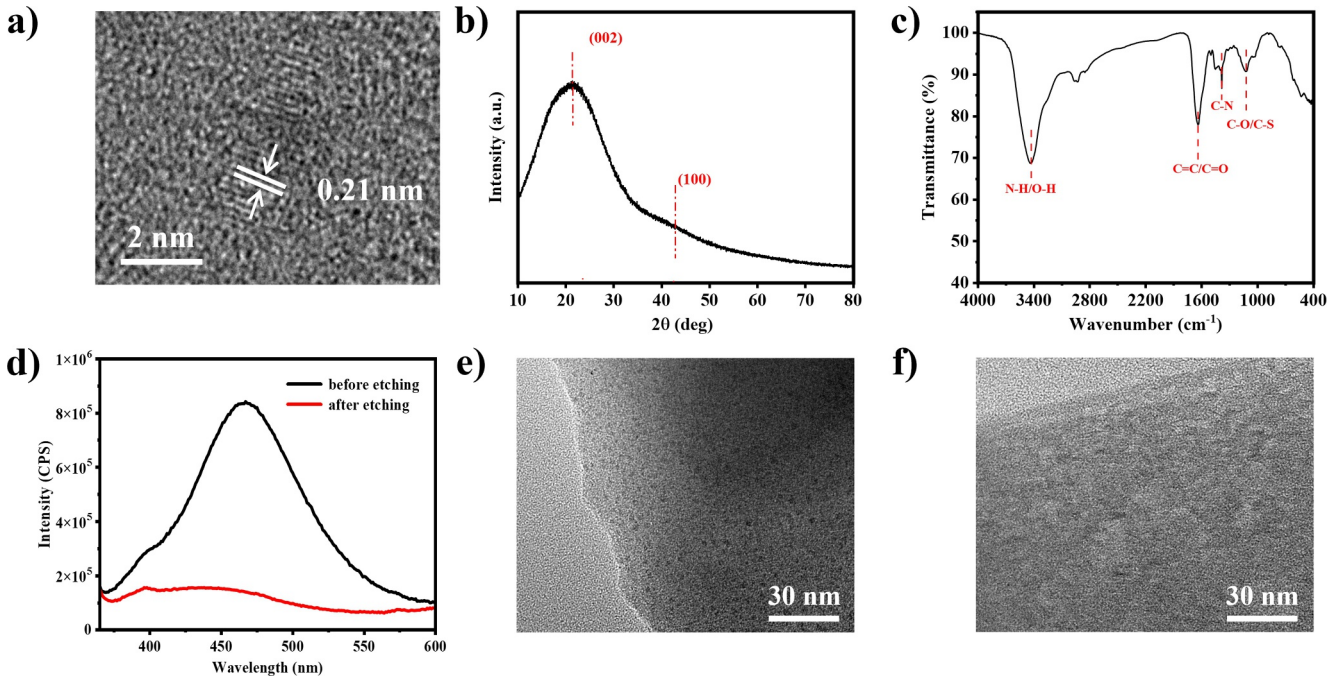

FIGURE 1 (a) High-resolution transmission electron microscopy image, (b) X-ray diffraction pattern and (c) Fourier transform infrared spectrometer spectrum of NSCDs. (d) PL spectra of NSCDs before and after etching. Transmission electron microscopy images of NSCD@PH-0.5 (e) before and (f) after KOH etching. NSCDs, nitrogen-sulfur co-doped carbon dots.

sample, respectively. In the high-resolution spectra, the N 1s peak (Supporting Information S1: Figure S1a) can be deconvoluted into three distinct peaks at 398.6, 399.6, and 401 eV, which correspond to pyridinic N, pyrrolic N, and graphitic N respectively, with the first two being predominant.[25] The O 1s peak consists of three components: S-O, C=O, and C−O, located at 530.4, 531.4, and 532.6 eV, respectively (Supporting Information S1: Figure S1b).[26] The minimal proportion of C-O suggests that the NSCDs are highly amidized, and the prominent S-O peak reflects the high oxidation state of sulfur. The S 2p spectrum shows three components at 162.8, 164.1, and 167.3 eV, corresponding to -C-S-, -S-S-, and C-SO_x-C bonds (Supporting Information S1: Figure S1c).[27,28] Coupled with the O 1s spectrum, it can be inferred that during NSCDs formation, the thiol groups of L-cysteine undergo oxidation, facilitating the escape of sulfur as SO_2 at elevated temperatures. In addition, the morphology and elemental composition of NSCD@PH-0.5

were examined by scanning electron microscopy (SEM) and energy dispersive spectroscopy (EDS). As shown in Supporting Information S1: Figure S2, the elements C, N, O, and S are uniformly distributed, confirming the homogeneous presence of NSCDs in the hydrogel. TEM images of NSCD@PH-0.5 before (Figure 1e) and after (Figure 1f) etching show that the after etching the hydrogel becomes porous and the nanoparticles disappear in the whole material. These results confirm that the tiny pores in hydrogel are produced by etching NSCDs in KOH solution.

The morphologies of the CPH-x products (where $x = 0.4$, 0.5, 0.6, and 0.7, corresponding to the amounts of NSCDs introduced into the hydrogel, accounting for approximately 18%, 22%, 25%, and 28% of the total mass of the hydrogel matrix, respectively), were studied via SEM and TEM, respectively. When the NSCDs amounts are 0.4 and 0.5 g (Figure 2a,b), a significant number of macropores are observed, with CPH-0.5 exhibiting an even higher quantity. However, when the NSCDs amounts are increased to 0.6 and 0.7 g (Figure 2c,d), the macropores nearly disappeared, and only a few large pores were observed in CPH-0.6. At lower contents of NSCDs, the interactions between the NSCDs and PEGDGE are insufficient, limiting the pore-forming ability. Conversely, at higher concentrations of NSCDs, the aggregation of multiple NSCDs will contribute to forming a single pore, resulting in larger pore sizes and limited SSA. Notably, regardless of the NSCDs amount, a significant number of mesopores are observed in the TEM images (Figure 2e–h), a feature originating from both the inherent characteristics of the NSCDs and the contribution of $ZnCl_2$, which will be further discussed in the subsequent pore size distribution analyses.

XPS analyses (Figure 3) reveal the chemical composition and electronic structure of the porous carbon materials. It shows that all CPHs retain high levels of oxygen and trace amounts of nitrogen in their carbon frameworks, which typically enhance the materials' hydrophilicity and pseudocapacitive performance, making them particularly suitable for electrochemical supercapacitors.[29] The high-resolution N 1s spectrum consisted of four peaks corresponding to pyridinic N, pyrrolic N, graphitic N, and oxidized N,

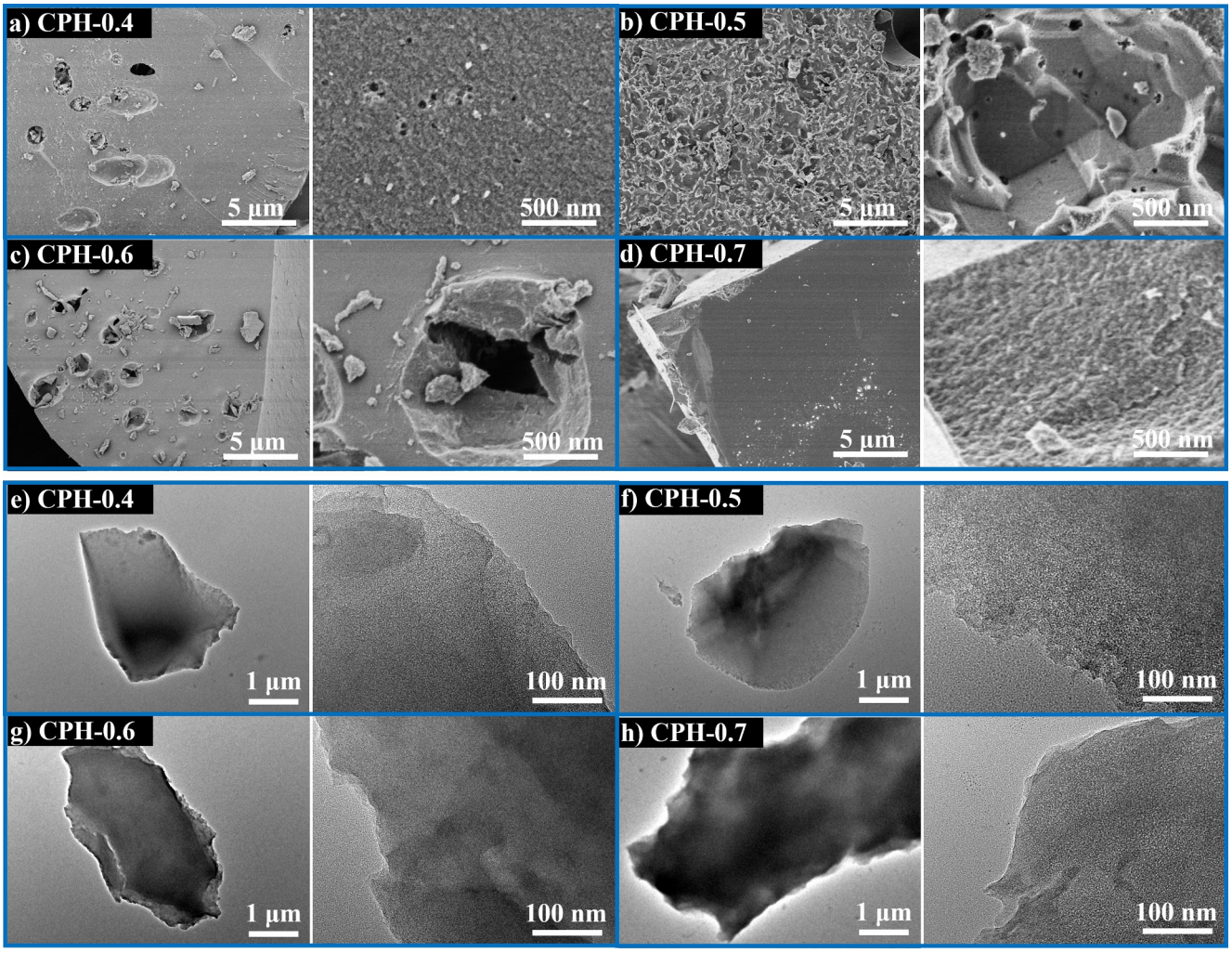

FIGURE 2 Scanning electron microscopy images of (a) CPH-0.4, (b) CPH-0.5, (c) CPH-0.6 and (d) CPH-0.7, respectively. Transmission electron microscopy images of (e) CPH-0.4, (f) CPH-0.5, (g) CPH-0.6 and (h) CPH-0.7, respectively. CPH, carbonized polymer hydrogel.

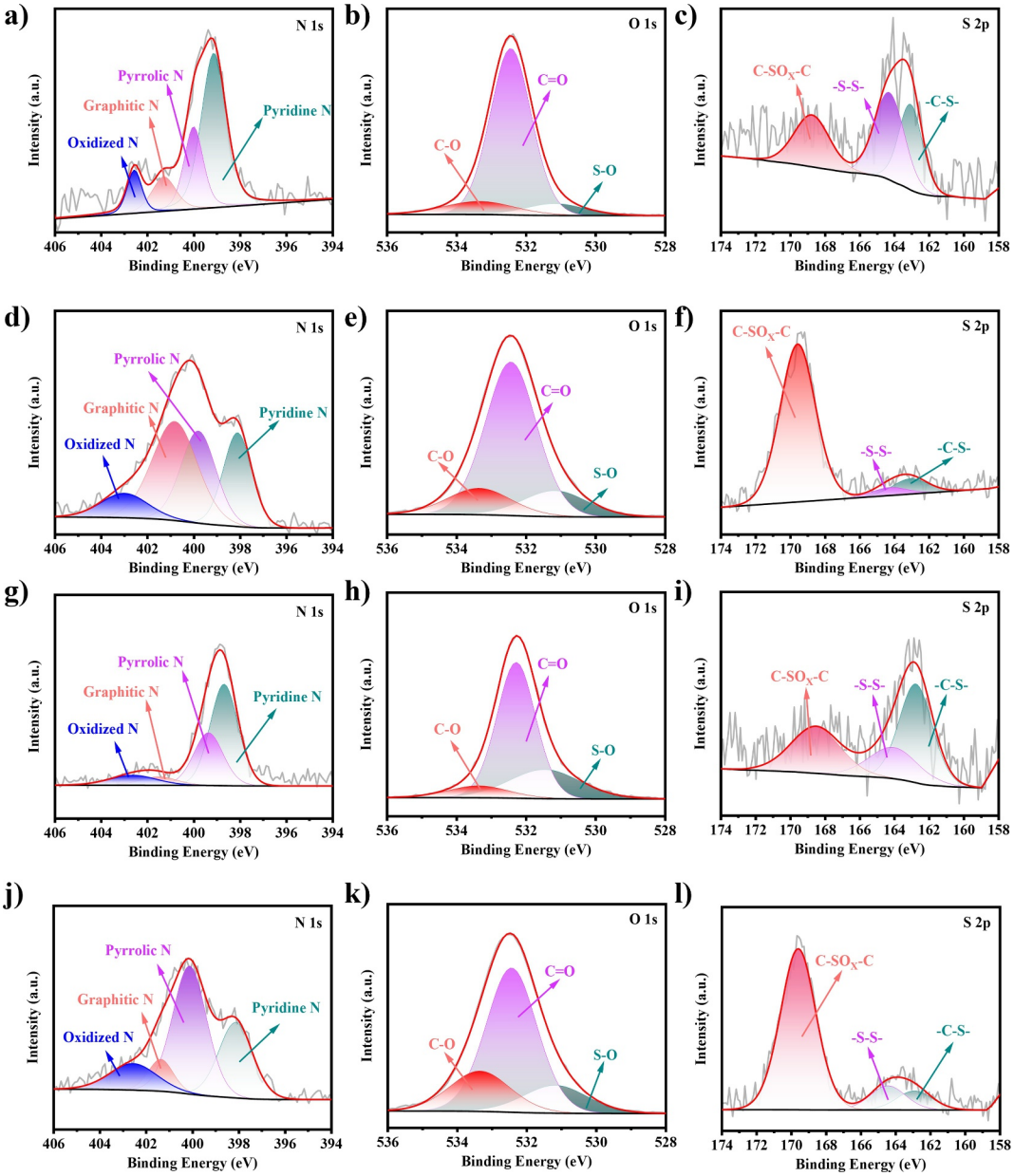

FIGURE 3 Core-level X-ray photoelectron spectra spectra of N 1s, O 1s and S 2p for (a-c) CPH-0.4, (d-f) CPH-0.5, (g-i) CPH-0.6 and (j-l) CPH-0.7, respectively. CPH, carbonized polymer hydrogel.

respectively. It has been reported that pyridinic N and pyrrolic N are often associated with electron-rich sites that facilitate ion insertion and extraction and K^+ ions storage capability, while graphitic N has been reported to improve electron delocalization, enhancing the electrical conductivity of the material.[30,31] The CPHs all exhibit elevated levels of pyrrolic N and pyridinic N, while CPH-0.5 shows a notably higher proportion of graphitic N, suggesting that it may possess superior rate performance for supercapacitors. The O 1s spectrum demonstrate that all samples have similar O species, primarily in the form of C=O bonds. These oxygen functionalities are crucial for improving surface reactivity, which can enhance ion adsorption, and thereby increase the pseudocapacitance of the material. The S 2p spectrum showed three distinct bonding states: C-S (S 2p 3/2), S-S (S 2p 1/2), and C−SO_x−C.[32] The prominent C−SO_x−C peak, coupled with the extremely low sulfur content in the carbon framework (mostly <1%, Supporting Information S1: Table S1), supports the hypothesis mentioned earlier in Scheme 1, indicating that S species escape in the form of SO_x gases. The high temperature treatment likely leads to the volatilization of sulfur, leaving behind a relatively sulfur-free carbon framework. This process is commonly observed in the synthesis of porous carbons, where the escape of volatile species takes place during the thermal activation.

To investigate the formation mechanism of micropores in depth, N_2 adsorption/desorption experiments were conducted to analyze the pore structure and quantity of CPHs and the Control group (Supporting Information S1: Table S2), while other porous carbon materials reported were listed for

comparison (Supporting Information S1: Table S3). As shown in Supporting Information S1: Figure S3, the pore sizes of these CPHs samples depend critically on the preparation conditions. Similar with the preparation for CPH-0.5, $ZnCl_2$ was omitted while all other conditions were kept unchanged, yielding Control I, which exhibited a low SSA and a similar pore size distribution as the CPHs samples. This indicates that $ZnCl_2$ primarily serves to increase the SSA of the porous carbon here, rather than being a key factor in establishing the characteristic pore-size feature. Based on the procedure for Control I, the 90°C environment required for alkaline etching was replaced with room temperature, resulting in minimal amide-bond cleavage, and the obtained sample was named Control II, which underwent neither etching-induced pore formation nor $ZnCl_2$ activation showing significantly poor pore performance. The ultralow SSA (1.13 $m^2\ g^{-1}$) of Control II not only ruled out any potential effects arising from residual KOH, but also clearly demonstrated the pivotal role of amide-bond etching in pore formation. Finally, when $ZnCl_2$ was reintroduced as an activator into the procedure of Control II, Control III was obtained, which exhibited a distinct pore distribution compared to the CPHs and Control I. Control III indicated that, when pore formation via amide-bond cleavage was suppressed, $ZnCl_2$ activation alone produced only a broad pore-size distribution predominantly below 1 nm. All these Control experiments indicate that $ZnCl_2$ activation mainly increases SSA and contributes to additional pore volume, whereas the characteristic pore-size feature (peak centered at 1.1–1.6 nm and the promoted mesopore fraction) is primarily governed by the NSCD-mediated etching–gasification synergy.

Figure 4a shows the pore sizes of all CPH-x samples are primarily concentrated in the range of 1.1–1.6 nm. They exhibit the Type IV adsorption isotherm at low relative pressures ($P/P_0 < 0.01$), with a characteristic hysteresis loop, indicating a rich mesopore structure (Figure 4b). Among them, CPH-0.5 has the highest SSA of 933 $m^2{\cdot}g^{-1}$ (Figure 4c), while the SSAs of CPH-0.4, CPH-0.6, and CPH-0.7 are 909, 805, and 778 $m^2{\cdot}g^{-1}$, respectively, in accord with the results in Figure 2. In contrast, the SSAs of Control I, II, and III are only 427, 113, and 612 $m^2{\cdot}g^{-1}$, respectively, highlighting the advantage of the NSCDs self-template in preparing porous carbon of high surface area. Alkali etching first introduces pre-formed pores and a high density of defects into the hydrogel network, providing a structural starting point for pore expansion. During carbonization, sulfur-containing functional groups undergo substantial removal and release gaseous species, which promotes pore widening and coalescence. $ZnCl_2$ creates a salt-phase occupying effect, and subsequent leaching leaves behind a connected pore volume. As Figure 4d shows, the synergistic interplay of these factors drives the pore structure to evolve toward an impressive mesopore volume ratio (up to 47.2%), breaking the previous limitation of CDs as only templates for sub-nanometer pore structures. The XRD patterns of the CPHs show a broad and low-intensity diffraction peak around 25°, indicating an amorphous porous nature (Supporting Information S1: Figure S4).[33] The Raman spectra exhibit characteristic D-band (1351 cm^{-1}) and G-band (1600 cm^{-1}) peaks (Figure 4e), representing the disordered and the graphitic vibrations in the carbon material, respectively. The high I_D/I_G ratio results from the poor ordering of

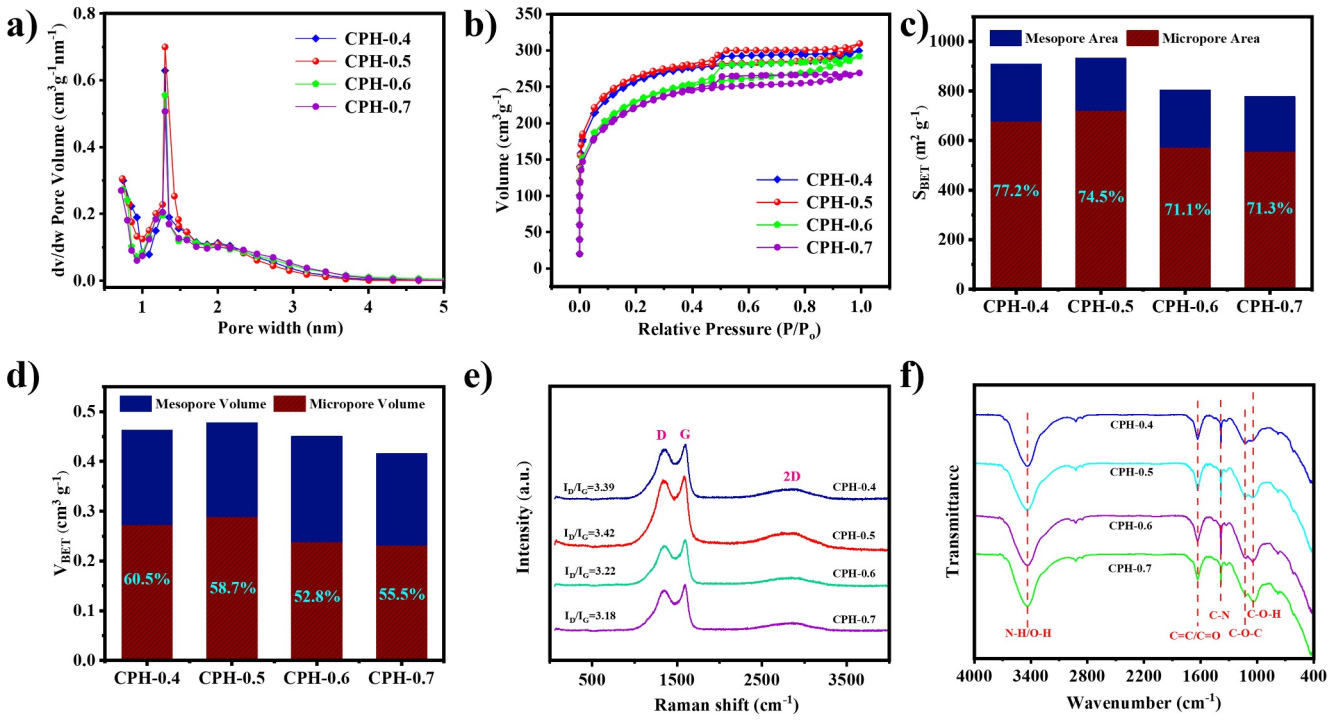

FIGURE 4 (a) Pore size distributions, (b) nitrogen adsorption-desorption isotherm, (c) specific surface areas, (d) specific pore volumes, (e) Raman spectra and (f) FT-IR spectra of carbonized polymer hydrogels, respectively.

the carbon structure, typical of highly porous and curved carbon frameworks with heteroatom substitution. The changing trend of the I_D/I_G value is consistent with the SSA of the CPHs, which confirms that only an appropriate amount of NSCDs can maximize the increase of defects in the porous carbon material.[17,34] FTIR analysis reveals that the CPHs samples are rich in N-H/O-H, C-O, and C-N functional groups, which provide excellent wettability and additional capacitance for the electrode materials (Figure 4f).[35] Additionally, it is observed that with an increasing amount of NSCDs, the intensity of the C-O-H stretching vibration peak gradually increases, because the greater number of NSCDs facilitates a more complete ring-opening reaction of PEGDGE, resulting in a higher content of alcohol groups in the final product.

Electrochemical characterizations of the CPHs, including cyclic voltammetry (CV), galvanostatic charge/discharge (GCD), and electrochemical impedance spectroscopy (EIS), were conducted using a three-electrode system with a 6 M KOH aqueous electrolyte (Figure 5a–e and Supporting Information S1: Figure S5–S7). Under a scan rate of 50 mV s^{-1}, all CV curves exhibited a quasi-rectangular shape with a slight reversible hump (Figure 5a), indicative of typical electric double layer capacitor (EDLC) behavior, with a small contribution from pseudocapacitance due to the reversible redox reactions of N/O functional groups. In alkaline conditions, the hydrophilicity of N/O functional groups facilitates the insertion and removal of hydrated ions into the porous structure, contributing to pseudocapacitance.[36] Among the samples, CPH-0.5 displayed the largest CV integral area, corresponding to the highest charge storage capacity, in line with its elevated S_{BET} and abundant micropore structure. The GCD curves for each sample at a current density of 1 A g^{-1} are shown in Figure 5b, where all curves are nearly isosceles triangles with a negligible IR drop (~3 mV). From these GCD curves, the specific capacitances at 1 A g^{-1} were calculated for each electrode. The CPH-0.5 electrode exhibited the highest gravimetric capacitance at 386 F g^{-1}, while CPH-0.4, CPH-0.6, and CPH-0.7 electrodes had specific capacitances of 344, 318, 302, and 247 F g^{-1}, respectively. Furthermore, Figure 5c and Supporting Information S1: Figure S5 display the CV curves of CPH-0.5 and other electrodes at various scan rates, while Figure 5d and Supporting Information S1: Figure S6 show the GCD curves at different current densities. The rectangular CV curves at high scan rates and symmetric GCD curves at high current densities confirm the reversibility and efficiency of the ion adsorption/desorption process, highlighting the capacitive advantages of these materials.

To further assess the energy storage capabilities of CPHs, their capacitance retention rates at different current densities are presented in Figure 5e, respectively. CPH-0.5, with its higher graphite N content, demonstrates superior performance, maintaining a capacity of 309 F g^{-1} even at a high current density of 20 A g^{-1}. As shown in Figure 5f, after 10,000 cycles at 5 A g^{-1}, CPH-0.5 retains 94.8% of its initial capacitance and nearly 100% of Coulombic efficiency, demonstrating excellent cycling stability. The typical performance parameters of CPH-0.5 are further validated by

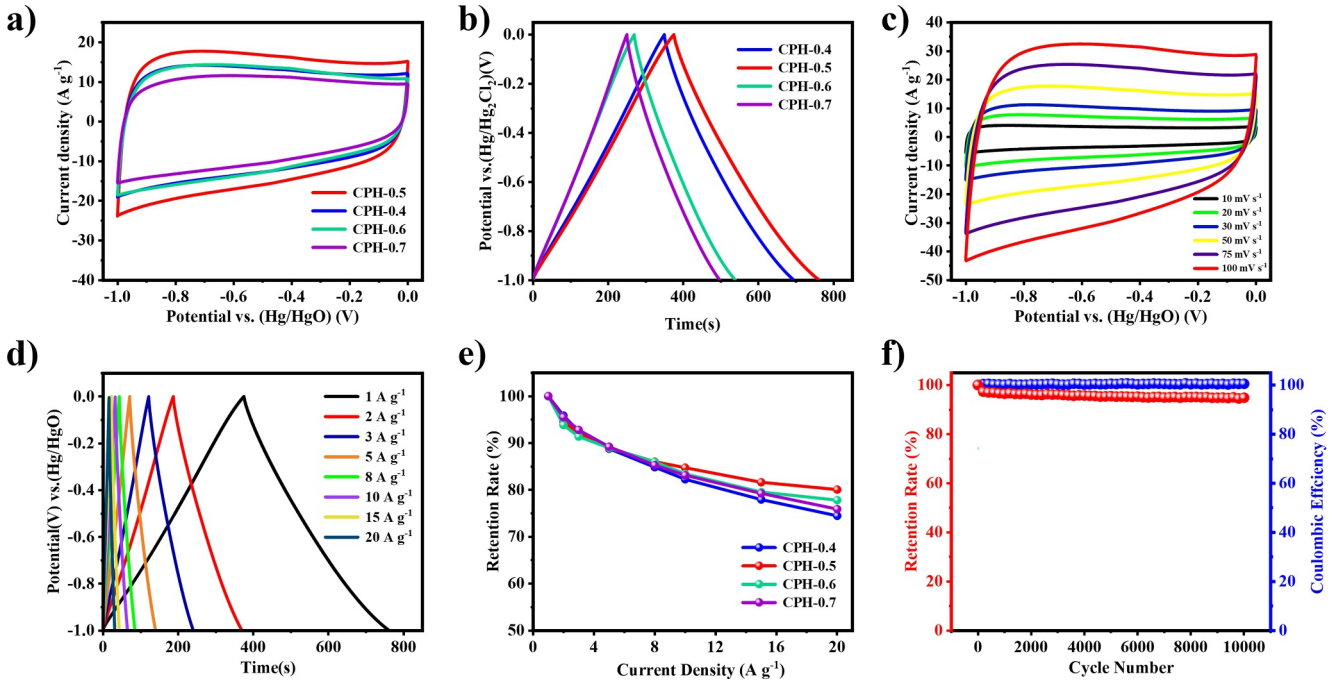

FIGURE 5 Electrochemical performances of CPHs tested via a three-electrode system. (a) CV curves at scan rates of 50 mV s^{-1} and (b) GCD curves at 1 A g^{-1}. (c) CV curves of CPH-0.5 at various scan rates. (d) GCD curves of CPH-0.5 at various current densities. (e) The rate performance at various current densities. (f) Cycling stability and Coulombic efficiencies of CPH-0.5 for 10,000 cycles at 5 A g^{-1}. CPHs, carbonized polymer hydrogels; GCD, galvanostatic charge/discharge.

comparison with other porous carbon materials in the literature (Supporting Information S1: Table S4).[37–46] Additionally, EIS analyses were performed to investigate the ion diffusion and transport kinetics of electrolytes in these samples. Supporting Information S1: Figure S7a reveals that all Nyquist plots exhibit steep linear curves in the low-frequency region, corresponding to the ideal capacitive behavior, and semicircles at high frequencies, reflecting the internal and surface resistance. Supporting Information S1: Table S5 shows that CPH-0.5 exhibits the lowest resistance value and CPH-0.4 shows the highest one, consistent with the results in Figure 5e. In the Bode plot (Supporting Information S1: Figure S7b), all samples display a phase angle near −90° at low frequencies, that is a character of the capacitive behavior. Furthermore, the characteristic relaxation times (τ_0) calculated from f_0 (the frequency at half the maximum capacitance) for CPH-0.4, CPH-0.5, CPH-0.6, and CPH-0.7 are 4.2, 1.5, 1.1, and 1.9 s, respectively, indicating the fast charge/discharge performance can be attributed to the high mesopore contents in these samples.

A symmetric supercapacitor (SSC) was fabricated using the high-performance CPH-0.5 electrodes and 6 M KOH aqueous solution as the electrolyte, followed by CV testing. As shown in Figure 6a, the CV curves shift towards the sloped region with increasing scan rates, which can be attributed to the interference of higher impedance. However, even at a scan rate of 200 mV s^{-1}, the curves still maintain a quasi-rectangular shape, representing the good conductivity and fast ion transport capabilities of the sample. Additionally, the GCD curves of the SSC at various current densities are all near-symmetric triangles (Figure 6b), confirming the ideal electrochemical reversibility and Coulombic efficiency. In Figure 6c, the specific capacitances of the SSC at different current densities are calculated from the GCD data, 82 F g^{-1} at 1 A g^{-1} and 64 F g^{-1} at 10 A g^{-1} respectively, demonstrating the excellent rate performance. The Nyquist plot (Figure 6d) reveals small semicircles in the high-frequency region and a nearly vertical line in the low-frequency region, indicative of superior charge transfer dynamics and EDLC properties. Notably, after 10,000 charge-discharge cycles, the resistance corresponding to the semicircle changes minimally, and the line maintains a steep slope, demonstrating the stability of the porous carbon structure. The cycling stability of the SSC in the 6 M KOH electrolyte was further evaluated through GCD tests. As shown in Figure 6e, the specific capacitance of the SSC at 5 A g^{-1} retains 97% of its initial value after 10,000 cycles, indicating the excellent electrochemical cycle stability. The energy and power densities vary from 17.3 to 22.4 Wh kg^{-1} and from 700 to 7000 W kg^{-1}, respectively, which are competitive with other carbon materials using KOH electrolytes (Figure 6f).[38,39,41–44,46,47]

3 | CONCLUSION

In summary, we synthesized a series of hierarchical porous carbon materials by utilizing NSCDs as self-templates for pore formation. The NSCDs initially introduce primary porosity into the precursor through amide bond etching, followed by the thermal decomposition of sulfur-containing

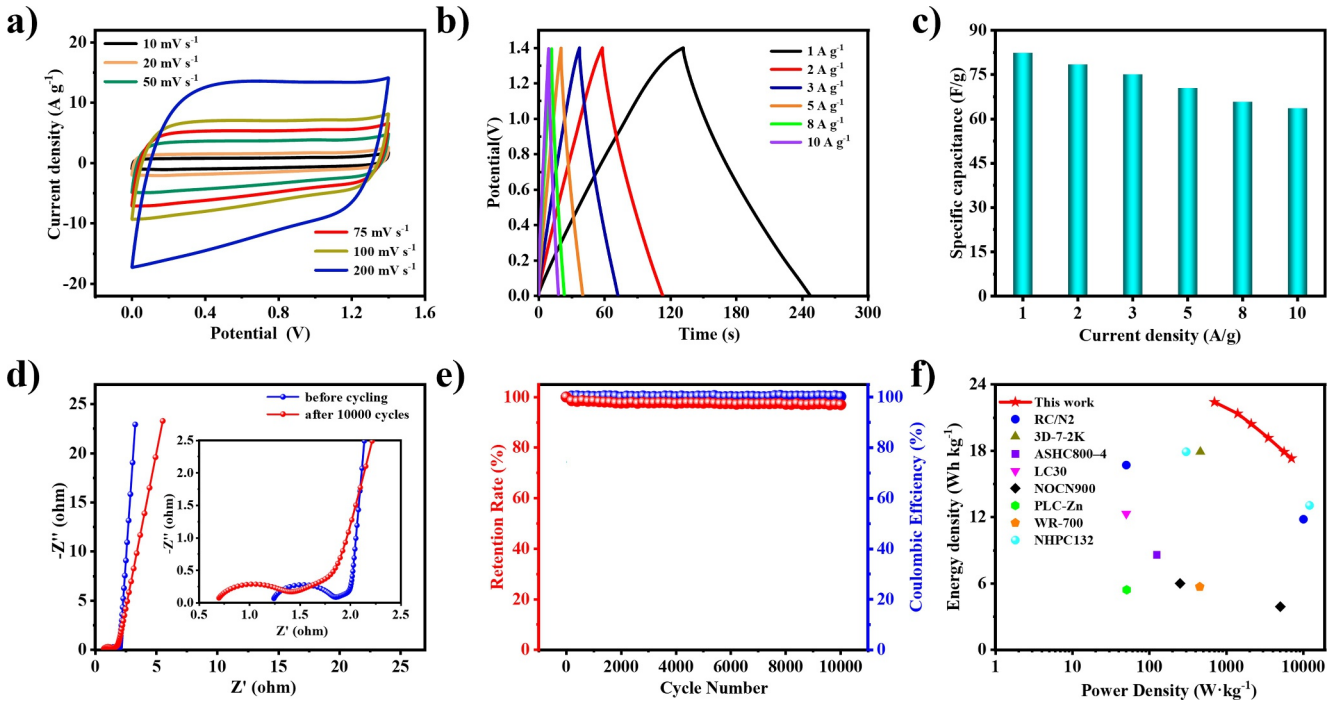

FIGURE 6 Electrochemical performances of the CPH-0.5‖CPH-0.5 symmetric supercapacitor in 6 M KOH electrolyte. (a) CV curves at various scan rates. (b) Galvanostatic charge/discharge curves and (c) specific capacitance at different current densities. (d) Nyquist plots before and after 10,000 cycles. (e) Cycling stability at 5 A g^{-1} after 10,000 cycles. (f) Ragone plot of power density versus energy density for CPH-0.5‖CPH-0.5 and other carbon-based devices. CPH, carbonized polymer hydrogel.

functional groups, which further enhances the pore size. This approach successfully generates the larger micropore size distribution centered around 1.1–1.6 nm and an ultrahigh mesopore volume ratio (up to 47.2%) in the resulting porous carbon, which addresses a longstanding limitation of CDs as self-templating agents for pore formation. Micropores with slightly larger diameters still provide sufficient ion adsorption sites, and their synergy with a high proportion of mesopores enhances ion transport kinetics. As a result, the optimal sample exhibits a capacitance of 386 F g^{-1} at 1 A g^{-1}, retaining 80% of its capacity at a high current density of 20 A g^{-1}. Additionally, the stable and easily reproducible pore structure, along with the ability to incorporate heteroatoms, highlights the potential of NSCDs as versatile self-templates for designing porous carbon materials for multifunctional requirements. This study offers a new perspective on the design of super-capacitive carbon materials by using CDs as self-templates. Since the internal structures and surface states of CDs can be adjusted and optimized critically, porous carbon materials derived from CDs assembly and decomposition will demonstrate rich structures and superior performance in the near future.

4 | EXPERIMENTAL SECTION

4.1 | Chemicals and materials

L-cysteine (L-Cys), Poly(ethylene glycol) diglycidyl ether (PEGDGE, M_n = 500), Polyethylenimine (PEI), and Polytetrafluorethylene preparation (PTFE) were obtained from Aladdin Reagent Co. (China). Hydrochloric acid, super P, potassium hydroxide, and zinc chloride were purchased from Sinopharm Chemical Reagent Co., Ltd (Shanghai, China).

4.2 | Synthesis of N, S co-doped carbon dots (NSCDs)

L-cysteine (L-Cys, 0.9 g) and polyethyleneimine (PEI, 1.0 g of 50 wt.% aqueous solution) were dissolved in deionized water (10 mL), and the resulting solution was transferred into a Teflon-lined stainless-steel autoclave, where it was heated at 180°C for 6 h. After cooling to room temperature, the obtained solution was purified via dialysis using a membrane with a molecular weight cutoff of 1500 Da. The product was then further dried at 80°C.

4.3 | Synthesis of hydrogels (NSCD@PHs)

Various amounts of NSCDs (0.4, 0.5, 0.6, 0.7 g) were mixed with 1.8 g of PEGDGE and dissolved in 3 mL of deionized water, followed by heating at 80°C for 12 h. The resulting hydrogel was washed with deionized water and then vacuum-dried at 80°C. These hydrogels were labeled as NSCD@PH-x (where x = 0.4, 0.5, 0.6, and 0.7), corresponding to the amount of NSCDs added.

4.4 | Synthesis of porous carbon (CPHs)

The previously synthesized NSCD@PH-x hydrogels (2 g) were each immersed in 20 mL of 2 M KOH aqueous solution and heated at 90°C for 24 h. The resulting samples were thoroughly washed with water and then dried at 80°C in vacuum. After weighing, the samples were swollen in an aqueous solution of zinc chloride with equal mass to that of the sample, followed by freeze-drying. After this treatment, the samples containing zinc chloride were placed in a tube furnace, heated at a rate of 5°C/min to 300°C, and held for 1 h. The temperature was then increased to 800°C at 2°C/min, maintaining 800°C for 2 h in nitrogen atmosphere. After cooling, the products were washed with 2 M HCl aqueous solution and deionized water, finally dried at 80°C, yielding porous carbon powder labeled as CPH-x (where x = 0.4, 0.5, 0.6, and 0.7, respectively).

4.5 | Synthesis of control I, II, and III

For comparison, a NSCD@PH-0.5 hydrogel was treated following the same procedure as the experimental group, except that no zinc chloride was used. The resulting porous carbon was labeled Control I. Another batch of NSCD@PH-0.5 hydrogel was divided into two groups. Both were placed in 20 mL of 2 M KOH solution and soaked at room temperature for 24 h before being thoroughly rinsed with water. One group continued with the experimental procedure, but without the addition of zinc chloride. The resulting porous carbon product was labeled Control II. The other group followed the exact same process as the experimental group, and the resulting product was labeled Control III.

4.6 | Instruments

SEM were imaged on FlexSEM 1000 (Japan). Field Emission TEM and HRTEM images were collected from a Tecnai G2 F20 S-Twin electron microscope operating at 200 kV. XRD patterns were conducted on Bruker D2 PHASER diffractometer. Fourier Transform Infrared Spectrometer (FTIR) spectra were recorded on a Nicolet iS10 spectrometer. X-ray photoelectron spectroscopy (XPS) data was analyzed using a PHI 5000C&PHI5300 spectrometer. The fluorescence spectra were investigated on a Horiba Jobin Yvon FluoroMax-4 spectrofluorometer with an F-3018 integrating sphere. Raman spectra were measured on Renishaw inVia Raman spectrometers. Nitrogen adsorption-desorption curves were collected by Micromeritics ASAP 2460.

4.7 | Electrochemical measurements

To prepare the working electrodes, the as-prepared porous carbon, Super P, and PTFE binder were blended in a mass ratio of 8:1:1. This mixture was then pressed onto a stainless-steel mesh with a surface area of 1 cm^2 and dried at 80°C for 24 h. The mass loading on a single electrode is approximately 1 mg cm^{-2}. The electrochemical tests were conducted using a three-electrode system, where the Hg/HgO electrode served as the reference, Pt foils were used as the counter electrodes, and 6 M KOH solution acted as the electrolyte. The tests were performed within the potential range of −1.0 to 0 V. For the symmetric supercapacitor (SSC), two CPH-0.5 electrodes were assembled as described above and tested in 6 M KOH within the voltage window of 0–1.4 V. All cyclic voltammetry (CV) and EIS measurements (covering a frequency range from 0.01 to 100 kHz) were conducted using a CHI 660E electrochemical workstation. Galvanostatic charge-discharge (GCD) tests were performed with a CT2001A Land cell tester.

The gravimetric capacitance (C_s) in three-electrode system and symmetric supercapacitor was calculated from the galvanostatic discharge curves, based on the active material mass, using the following equation:

$$C_s = \frac{I\Delta t}{m\Delta V} \quad (1)$$

where I (A), ΔV (V) and Δt (s) represent the discharge current, voltage window, and discharge time, respectively. Notably, m (g) is the mass of active material on the working electrode in three-electrode system, while it refers to the total mass of active material on two electrodes in the CPH-0.5|| CPH-0.5 symmetric supercapacitor.

The energy density (E_g, Wh kg^{-1}) and power density (P_g, W kg^{-1}) were derived from the GCD curves of the SSC using the equations below:

$$E_g = \frac{1}{2 \times 3.6} C_s \Delta V^2 \quad (2)$$

$$P_g = \frac{E_g \times 3600}{\Delta t} \quad (3)$$

AUTHOR CONTRIBUTIONS

Xi-Rong Zhang: Methodology; software; validation; formal analysis; investigation; data curation; visualization; writing—original draft. **Hao-Wen Sun**: Software; validation; formal analysis; investigation. **Ling Xiao**: Investigation; data curation; visualization. **Zhao-Fan Wu**: Software; data curation. **Huan-Ming Xiong**: Conceptualization; supervision; funding acquisition; project administration; resources; writing—review and editing.

ACKNOWLEDGMENTS

This work was financially supported by the National Natural Science Foundation of China (U24A20565, 22575057) and the Science and Technology Commission of Shanghai Municipality (25ZR1401024).

CONFLICT OF INTEREST STATEMENT

The authors declare no conflict of interest.

DATA AVAILABILITY STATEMENT

The data that supports the findings of this study are available in the supporting information of this article.

ORCID

Huan-Ming Xiong https://orcid.org/0000-0002-3118-942X

REFERENCES

1. Q. Wang, Y. X. Qu, Y. X. Yuan, Z. Y. Chen, G. L. Feng, P. P. Dong, X. X. Jiao, Y. L. Zou, W. Q. Yang, *Adv. Mater.* **2025**, *37*, 202418997.
2. J. C. Lu, X. Y. Zhong, X. M. Lin, J. Q. Gui, M. T. Zheng, Y. L. Liu, Y. R. Liang, *Energy Environ. Sci.* **2024**, *17*, 6833.
3. W. W. Fan, Z. Sun, *Responsive Mater.* **2025**, *3*, e70019.
4. V. Pavlenko, S. Khosravi, S. Zoltowska, A. B. Haruna, M. Zahid, Z. Mansurov, Z. Supiyeva, A. Galal, K. I. Ozoemena, Q. Abbas, T. Jesionowski, *Mater. Sci. Eng. R Rep.* **2022**, *149*, 100682.
5. V. Malgras, J. Tang, J. Wang, J. Kim, N. L. Torad, S. Dutta, K. Ariga, M. S. A. Hossain, Y. Yamauchi, K. C. W. Wu, *J. Nanosci. Nanotechnol.* **2019**, *19*, 3673.
6. L. Sun, Y. N. Gong, D. L. Li, C. X. Pan, *Green Chem.* **2022**, *24*, 3864.
7. S. Li, H. Zhang, S. Li, J. Q. Wang, Q. W. Wang, Z. L. Cheng, *Renew. Sust. Energ. Rev.* **2024**, *202*, 114641.
8. R. W. Fu, Z. H. Li, Y. R. Liang, F. Li, F. Xu, D. C. Wu, *New Carbon Mater.* **2011**, *26*, 171.
9. T. Wang, P. X. Ren, Q. Liu, Q. Zhang, Y. F. Zheng, D. Z. Jia, D. L. Wu, *Adv. Funct. Mater.* **2025**, *36*, e04092.
10. M. Sevilla, N. Díez, A. B. Fuertes, *ChemSusChem* **2021**, *14*, 94.
11. H. Q. Zhang, Y. P. Liu, S. N. Qu, *Responsive Mater.* **2024**, *2*, e20240012.
12. F. Wang, R. Lyu, H. W. Xu, R. Gong, B. F. Ding, *Responsive Mater.* **2024**, *2*, e20240007.
13. M. Y. Lei, Q. Wang, R. R. Gu, D. H. Qu, *Responsive Mater.* **2024**, *2*, e20230027.
14. W. C. Gao, J. Qiao, J. M. Hu, Y. S. Guan, Q. Li, *Responsive Mater.* **2024**, *2*, e20230022.
15. J. S. Wei, T. B. Song, P. Zhang, X. Q. Niu, X. B. Chen, H. M. Xiong, *Mater. Chem. Front.* **2020**, *4*, 729.
16. H. Sentjens, A. J. J. Kragt, A. Schenning, M. G. Debije, *Responsive Mater.* **2023**, *1*, e20230006.
17. J. Huang, C. Liu, Y. Z. Jin, J. C. Chen, *Chem. Eng. J.* **2023**, *461*, 141930.
18. X. R. Zhang, B. J. Wang, H. W. Sun, Y. G. Wang, H. M. Xiong, *Angew. Chem. Int. Ed.* **2025**, *64*, 202519704.
19. X. R. Zhang, T. B. Song, T. L. He, Q. L. Ma, Z. F. Wu, Y. G. Wang, H. M. Xiong, *Adv. Funct. Mater.* **2025**, *35*, 202419219.
20. D. W. Boukhvalov, V. Y. Osipov, D. Murzalinov, A. Serikkanov, H. Bi, *Carbon* **2024**, *225*, 119101.
21. H. Ding, S. B. Yu, J. S. Wei, H. M. Xiong, *ACS Nano* **2016**, *10*, 484.
22. H. Y. Yang, Y. L. Liu, Z. Y. Guo, B. F. Lei, J. L. Zhuang, X. J. Zhang, Z. M. Liu, C. F. Hu, *Nat. Commun.* **2019**, *10*, 1789.
23. W. Q. Kong, J. Liu, R. H. Liu, H. Li, Y. Liu, H. Huang, K. Y. Li, J. Liu, S. T. Lee, Z. H. Kang, *Nanoscale* **2014**, *6*, 5116.
24. D. Sun, R. Ban, P. H. Zhang, G. H. Wu, J. R. Zhang, J. J. Zhu, *Carbon* **2013**, *64*, 424.
25. J. C. Li, X. P. Qin, P. X. Hou, M. Cheng, C. Shi, C. Liu, H. M. Cheng, M. H. Shao, *Carbon* **2019**, *147*, 303.
26. Y. J. Huang, X. Y. Hu, Y. J. Li, X. Zhong, Z. D. He, Z. L. Geng, S. Y. Gan, W. T. Deng, G. Q. Zou, H. S. Hou, X. B. Ji, *Adv. Funct. Mater.* **2024**, *34*, 12.

27. R. Q. Cheng, M. Jiang, K. Q. Li, M. L. Guo, J. Zhang, J. M. Ren, P. Y. Meng, R. H. Li, C. P. Fu, *Chem. Eng. J.* **2021**, *425*, 130603.
28. H. Ding, J. S. Wei, H. M. Xiong, *Nanoscale* **2014**, *6*, 13817.
29. P. Hao, Z. H. Zhao, Y. H. Leng, J. Tian, Y. H. Sang, R. I. Boughton, C. P. Wong, H. Liu, B. Yang, *Nano Energy* **2015**, *15*, 9.
30. H. N. He, D. Huang, Y. G. Tang, Q. Wang, X. B. Ji, H. Y. Wang, Z. P. Guo, *Nano Energy* **2019**, *57*, 728.
31. Y. H. Xie, Y. Chen, L. Liu, P. Tao, M. P. Fan, N. Xu, X. W. Shen, C. L. Yan, *Adv. Mater.* **2017**, *29*, 1702268.
32. J. Q. Yang, X. L. Zhou, D. H. Wu, X. D. Zhao, Z. Zhou, *Adv. Mater.* **2017**, *29*, 1604108.
33. T. Wang, J. Guo, Y. Guo, J. Feng, D. L. Wu, *ACS Appl. Energy Mater.* **2021**, *4*, 2190.
34. S. Wu, X. T. Yan, X. Sun, S. Tian, J. J. Wang, C. Y. Liu, S. Q. Sun, L. Wu, X. F. Zhao, Q. L. Yang, *J. Energy Storage* **2023**, *71*, 108152.
35. S. Ghosh, G. Pagani, A. Macrelli, A. Calloni, G. Bussetti, A. Lucotti, M. Tommasini, R. Suriano, M. Agozzino, G. Divitini, Y. P. Ivanov, V. Piazza, V. Russo, A. M. Jastrzebska, C. Casiraghi, A. Li Bassi, C. S. Casari, *Chem. Eng. J.* **2025**, *520*, 166402.
36. G. Y. Zhao, C. Chen, D. F. Yu, L. Sun, C. H. Yang, H. Zhang, Y. Sun, F. Besenbacher, M. Yu, *Nano Energy* **2018**, *47*, 547.
37. M. Wu, S. Xu, X. Li, T. K. Zhang, Z. Z. Lv, Z. G. Li, X. L. Li, *J. Energy Storage* **2021**, *40*, 102663.
38. Z. X. Guo, Z. W. Tian, G. G. Duan, Q. L. Fu, C. M. Zhang, X. S. Han, H. Q. Yang, S. J. He, S. H. Jiang, *Chem. Eng. J.* **2024**, *501*, 157702.
39. H. S. Li, F. Y. Shi, Q. D. An, S. R. Zhai, K. Wang, Y. Tong, *Int. J. Biol. Macromol.* **2021**, *166*, 923.
40. Q. Q. Qin, J. Z. Wang, Z. Y. Tang, Y. Jiang, L. Wang, *Ind. Crops Prod.* **2024**, *208*, 117878.
41. M. Huang, K. Huang, L. Zhao, J. S. He, D. Tian, Y. J. Lei, J. M. Zou, F. Shen, *Ind. Crops Prod.* **2023**, *206*, 117607.
42. Y. Lin, C. Huang, C. X. Huang, Y. J. Deng, X. X. Zou, W. C. Ma, G. G. Fang, A. J. Ragauskas, *Adv. Compos. Hybrid Mater.* **2024**, *7*, 51.
43. F. T. Ran, X. B. Yang, X. Q. Xu, S. W. Li, Y. Y. Liu, L. Shao, *Chem. Eng. J.* **2021**, *412*, 128673.
44. P. X. Feng, H. Wang, P. P. Huang, L. J. Zhong, S. Y. Gan, W. Wang, L. Niu, *Chem. Eng. J.* **2023**, *471*, 144817.
45. P. Yang, D. Y. Zheng, P. H. Zhu, F. Jiang, X. T. Bi, *Chem. Eng. J.* **2023**, *472*, 144785.
46. I. L. Egun, B. Akinwolemiwa, H. Y. He, M. C. Ma, Z. F. Chen, G. Z. Chen, D. Hu, *Chem. Eng. J.* **2025**, *509*, 161386.
47. B. Peng, Y. W. Zhu, S. Chu, H. Y. Zhang, *Chem. Eng. J.* **2025**, *507*, 160551.

SUPPORTING INFORMATION

Additional supporting information can be found online in the Supporting Information section at the end of this article.

How to cite this article: X.-R. Zhang, H.-W. Sun, L. Xiao, Z.-F. Wu, H.-M. Xiong, *Responsive Mater.* **2026**, e70050. https://doi.org/10.1002/rpm2.70050